Optimal Sampling Geometries for TV-Norm Reconstruction of fMRI Data

Oliver M. Jeromin, *Student Member, IEEE*, Vince D. Calhoun, *Senior Member, IEEE*, and Marios S. Pattichis, *Senior Member, IEEE*

***Abstract*—This study explores the ability to reconstruct functional magnetic resonance imaging (fMRI) brain slices from a limited number of K-space samples. We use compressed sensing methods to reconstruct brain imaging activity using different K-space sampling geometries. To determine the optimal sampling geometry, we compute the reconstruction error. Here, for each geometry, we also estimate the optimal weighting parameters for the total variation (TV) norm and L-2 norm penalty functions. Initial results show that the optimal sampling geometry varies significantly as a function of the required reduction in K-space sampling density (for 60% to 90% reduction). Furthermore, the reconstructed fMRI slices can be used to accurately detect regions of neural activity from a largely reduced number of K-space samples.**

I. Introduction

With the promise of near exact reconstruction of compressible signals from a small number of random projections, compressed sensing (CS) has promising applications in sparse signal acquisition, reconstruction, and encoding. In the traditional sense of digital image acquisition, the quality of data reconstructions that can be achieved by a specific sensor or modality depends on the total number of data elements it can capture. Image compression algorithms in use today typically operate under the assumption that the user has possession of the full-resolution set of data, which is then encoded using a compression scheme. The reduced representation of the data is then transmitted or stored, and eventually reconstructed using a-priori knowledge about the compression scheme.

Viewing CS in the context of data compression, it can be thought of a method of obtaining information from data that has, by its method of collection, already been compressed. Along these lines, this work explores the effects of reduced K-space sampling of an MRI scanner and its effects on fMRI data analysis.

CS theory requires that the data that is sampled is both represented within a sparse basis, and that the samples that are collected exhibit a suitable level of incoherence, which can be achieved by transforming the MRI collected data into a sparse basis (in this case, using the Wavelet transform) and under sampling in a way that the samples are incoherent with respect to the sparsifying domain [1]. The second requirement, the incoherence of under-sampling artifacts, will depend on how the subset of frequency domain (K-space) is sampled. While some of the most astonishing results of CS assume that sampling is completely random within K-space, such sampling on an actual MRI system tends to be impractical. Due to the hardware and physiological constraints inherent to MRI, sampling trajectories must follow relatively smooth lines and curves [1]. For simplicity, we have constrained our sampling geometries to ones based on squares, covering all possible directions with a simple scanning geometry on a Cartesian coordinate system.

Previous studies have shown that an approximation to the gradient using finite differencing is well suited for two-dimensional data recovery [2]. This approximation is referred to as the total variation norm, which can be defined as

$$TV(X) = \sum_{x,y} \sqrt{\left|D_1 m(x,y)\right|^2 + \left|D_2 m(x,y)\right|^2} \,. \qquad (1)$$

In (1), $D_1 m = m(x,y) - m(x-1,y)$ and $D_2 m = m(x,y) - m(x,y-1)$ are the finite differences of X in both of its dimensions. The addition of a total variation term to the objective function solving an L-1 norm minimization problem has shown to improve image reconstruction [3].

fMRI is used to identify localized regions of activity within the brain by measuring the physiological changes due to the hemodynamic response to neuron activation. Since the process of blood oxygenation is constrained by physiology as

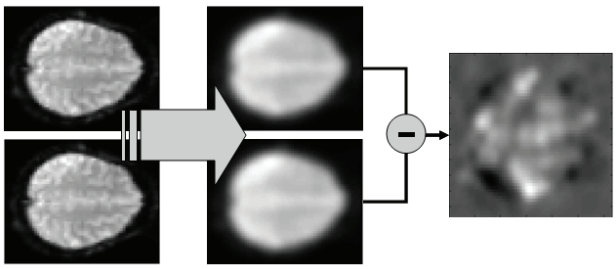

Fig. 1. The depiction of the sequence of steps required to detect brain activity. Two MRI images are acquired, one in which the subject is at rest, and another where the subject is performing a specific action. These two images are single slices of two separate brain scans. The images are both typically smoothed with a Gaussian kernel. The difference of the smoothed images reveals which spatial regions of the brain are active.

O Jeromin is with the Department of Electrical and Computer Engineering at the University of New Mexico, Albuquerque NM, 87131, USA. Mr. Jeromin is the corresponding author. He can be reached by phone at: 505-284-8119 or by e-mail: ojeromin@ece.unm.edu.

V.D. Calhoun is with the Department of Electrical and Computer Engineering at the University of New Mexico, and the Mind Research Network, Albuquerque NM, 87131, USA (e-mail: vcalhoun@unm.edu).

M.S. Pattichis is with the Department of Electrical and Computer Engineering at the University of New Mexico, Albuquerque NM, 87131, USA (e-mail: pattichis@ece.unm.edu).

well as the time required for the brain to process specified tasks, fMRI data tends to be more time consuming than spatial MRI imaging since the data consists of 3-D data sets that are being collected at different time points. A sample fMRI difference image is depicted in Fig. 1. We hope to explore the limitations of a CS solution on fMRI data collections, and our hope is that we can find a suitable reduction of K-space samples that provide sufficient fidelity in the difference image (task versus rest).

Our approach focuses on expanding the work described in [3], which developed K-space sampling techniques that focused on ensuring incoherence. We intend to present a set of sampling geometries that are intended to reduce the required number of samples and the complexity of the sampled geometry to reduce acquisition time. Adding (1) to an objective function that minimizes the L-1 norm of a transform operator, constraining the solution with an L-2 norm, and applying the optimal transform and TV penalties, the solution to our objective problem allows for improved reconstruction with less sophisticated geometries.

II. Theoretical Background

A. TV-Norm Reconstruction for Image Reconstruction

TV-Norm minimization is the key component to the problem of recovering data from a sparse basis. Compressed sensing lends itself well to image reconstruction from the Fourier, Wavelet, or other image transformations leading to sparse representations. A well-written overview of the reconstruction process can be found in [4], while the bulk of the theoretical aspects of this approach can be found in [5].

It has been shown that if the stated two conditions hold (sparsity and incoherence between samples), then with high probability the unknown signal components can be fully reconstructed [2,4,5].

B. Sparse MRI reconstruction

An overview of the possibilities CS lends to MRI image reconstruction can be found in [1]. Data samples generated by an MRI scanner are encoded using spatial-frequency encoding. The collected samples are transformed into an image by simply applying the two-dimensional inverse Fast Fourier Transform (FFT).

The sub-set of samples obtained from sparse data representations should also exhibit incoherence when reconstructed using a linear reconstruction method. This ensures that the non-linear reconstruction methods can detect the largest signal components during iterative reconstruction. Detailed analyses of various sampling methods designed to ensure incoherence between samples are described in [6-8]. Results from incoherent under-sampling in K-space provide strong support of the CS theory of sparsity and incoherence, but are often times impractical. In addition, MRI images tend to consist of pixels with a large dynamic range and considerable high-frequency components. The TV-Norm is an excellent candidate for reconstructing piece-wise constant signals, but tends to over-smooth the resulting pixel data. Therefore, a constraint is placed on (1), and the problem to solve becomes

$$\begin{aligned} \min \quad & \left\| \Psi x \right\|_{\ell_1} \\ s.t. \quad & \left\| \Im_u x - y \right\|_{\ell_2} \le \varepsilon \end{aligned} \tag{2}$$

Here, x is the reconstructed image, y are the measured K-space samples, and ε maintains a bound on the accuracy of the reconstructed data. The transformations, Ψ and F_u, represent the linear operator that transforms from pixel (reconstructed image) representation to the chosen sparse representation and the Fourier transform that under-samples the Fourier space data, respectively. Again, the objective function minimizes the TV-Norm. The L-2 norm in the constraint ensures that the solutions to the TV-Norm are consistent with the acquired data.

C. TV and Wavelet Transform Cost Parameters Selection

When considering sparse image reconstruction of data that is not piece-wise constant, the TV-Norm tends to underperform on its own. It has been shown that it is advantageous to include a TV penalty on the objective function in (2) [10]. Including this term leads to the optimization problem that is being solved in this work:

$$\begin{aligned} \min \quad & \beta \left\| \Psi x \right\|_{\ell_1} + \alpha TV\ (x) \\ s.t. \quad & \left\| \Im_u x - y \right\|_{\ell_2} \le \varepsilon . \end{aligned} \tag{3}$$

The TV penalty, α, as well as a transform penalty, β, allow for a compromise between the opposing effects of L-1 and L-2 norms in the objective function and the constraint.

The problem explored in this work examines the effects of varying the TV and transform penalties on reconstructed images using (3). The intention is to explore the feasibility of (3) as a solution to reconstruct a resting brain image and an image that contains neural activity. A non-linear conjugate gradient and backtracking algorithm described in [11] was used in solving (3). The fidelity of the CS reconstruction will be assessed based on the difference between the two images. It is this difference image that reveals to the observer which spatial regions within the brain are active.

III. METHODS

A. Selecting K-space Sampling Geometries

The feasibility of being able to accurately collect samples over a restricted K-space geometry led us to constrain the geometries to three separate classes. These are geometries consisting of a square region centered at the center of K-space. This class will be referred to as the "Centered Low Pass" (CLP) geometry. The second class is a combination of the CLP geometry and equidistant square patterns a single data sample wide and is referred to as the "Structured High Pass" (SHP) geometry. The third geometry contains a CLP region and variably spaced square patterns outside of the CLP region. This geometry is referred to as "Dyadic" (DY), and

its design is intended to sample high-frequency content at a varying amount based on how far the samples are from the center of K-space. Samples with a closer proximity to the K-space center will have a denser sampling pattern than those further displaced from the K-space center.

By varying the extent of the CLP class coverage and the spacing between the structured square patterns in the SHP class we were able to produce 81 unique geometries for analysis. Eight unique DY geometries were generated by varying the size of the CLP region, for a total of 89 geometries. Additionally, K-space sampling geometries were generated using uniform random sampling with various sample reduction rates ranging from 60%-95% sample reductions, as well as K-space sampling geometries that were generated using a sampling from a probability density function [9], bringing the total number of geometries to 103. These latter two methods ensure high incoherence among samples in the sparse basis, but would require more programming time during acquisitions.

B. Calculating Penalty Coefficients

For each of the above geometries, we employed the Nelder-Mead simplex algorithm to solve a two-dimensional unconstrained nonlinear minimization problem:

$$\min \sqrt{\frac{\sum_{i=1}^{n} (\hat{x}_i - x_i)^2}{n}}, \qquad (4)$$

$$\text{subject to } \hat{x} = \min \beta \left\| \Psi x \right\|_{\ell_1} + \alpha TV(x)$$

In (4), $\hat{x}$ is the solution to the non-linear convex problem in (3) and x is the spatial image obtained from the entire K-space samples. The α and β values are calculated using the search method described for a given geometry until a minimum the RMSE between the original, unsmoothed image and the result of (3) is found.

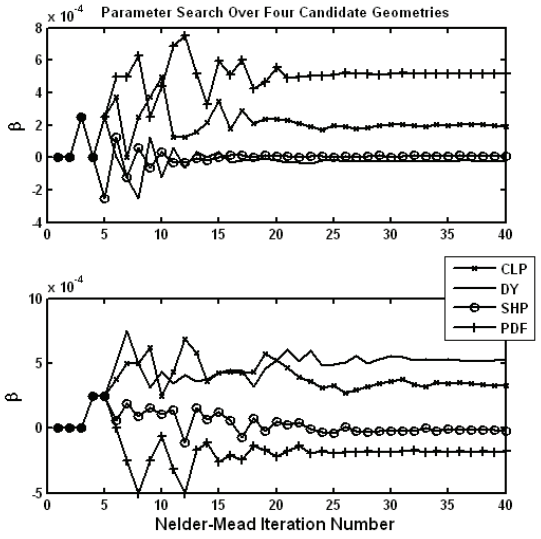

Fig. 2. These plots represent the α (top) and β (bottom) parameters at each Nelder-Mead search iteration for four selected geometries. Each plot converged to values that maximized the PSNR of the reconstructed image within 40 iterations.

C. Detection of Neural Activity

Neural activity in fMRI is typically detected by first smoothing the reconstructed active and at rest brain images with an 8mm half-power/half-bandwidth Gaussian kernel. The difference between the smoothed images results in a difference image where localized regions of activity in the brain can be segmented using a threshold followed by morphological processing. The threshold is selected as two standard deviations of the difference image data. The thresholding operation generates a noisy binary segmentation image. We use a morphological open operation (with a '+' structural element) to smooth the binary segmentation image.

The reconstructed imagery, which is the solution to (3) can also be used for analysis, if smoothing is not desired. Smoothing is used in the detection step because it provides leniency in the final detection error calculation.

IV. RESULTS

A. Optimal TV Coefficients using Nelder-Mead Search

TV minimization parameter coefficients were found that can be considered "optimal" in terms of producing a reconstructed image which minimized the RMSE between the result of (3) and the original brain images.

The α and β values were initially set to zero, which corresponds with the Fourier Transform solution of the reduced K-space data. Values corresponding with the minimum objective function in (4) ranged between -0.01 and 0.01 depending on the geometry being searched. The Nelder-Mead approach resulted in a unique minimum RSME solution for each of the 103 geometries studied. Figure 2 depicts the TV coefficients plotted against search iteration for a select geometry from the CLP, SHP, DY, and PDF classes. Poor performance by the Uniform class will be discussed further in the next section. All geometries exhibited convergence, albeit at various rates.

Future work is possible to further study the convergence of this method, as we make no claims as to whether the minima are global.

B. PSNR values of Searched Geometries

Peak Signal to Noise Ratio (PSNR) values were calculated using the minimized RMSE values produced by solving (4). Of the 103 geometries studied 41 exhibited PNR ratios greater than 30 dB, compared to just four geometries when no was performed.

One must also consider how much data reduction is achieved, as well as how well the missing K-space data is estimated. Therefore, it is noteworthy that 13 geometries having PSNR values over 30 dB and represented a K-space data reduction of 80% or greater. Figure 3 depicts the PSNR values sorted by the percent of data sampled. The best geometries in terms of PSNR from each of the four classes (CLP, SHP, DY, and PDF) are shown in Figure 4. Uniform

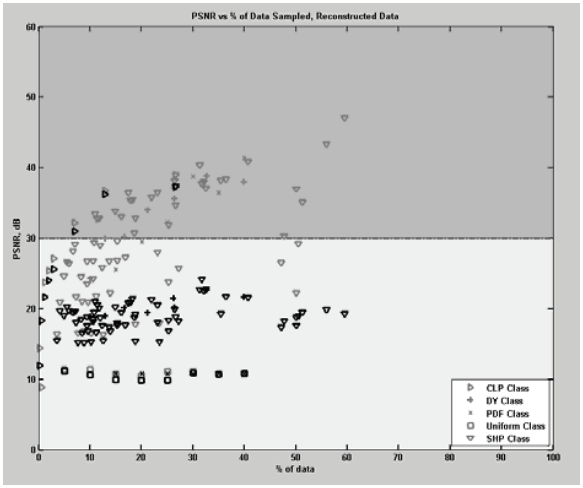

Fig. 3. Image reconstruction quality versus the percentage of K-space samples. We are interested in quality reconstructions (PSNR>30dB). The number of geometries that provide quality reconstructions increased from three geometries to forty-one geometries after reconstruction. The reconstructed PSNR values are denoted by the light grey plot markers, while the black markers represent no reconstruction.

sampling resulted in an average PSNR value of 10.96 dB, and will not be considered as a candidate. This result points to the need for sampling heavily in the DC portion of K-space, as is commonly done in image compression methods.

For a 60% reduction in the number of K-space data, the best PSNR value (41.39 dB) was achieved using the PDF geometries. Use of a Gibbs sampler to ensure high incoherence between samples ensures the geometry plays to the strengths of CS theory.

The other three geometries in Figure 4 pose special interest to this study, as they are easy to implement in an MRI scanner. The best CLP geometry in Figure 6 passed the K-space samples in a support of 50% of the samples in the phase-encoded dimension, and 50% of the samples in the frequency-encoded dimension.

Of the SHP geometry class, the best PSNR was achieved using the CLP geometry described above and square structures spaced 4 samples apart over the remaining K-space support. The best DY geometry had a central DC region covering 43% of K-space. The DC region encapsulated 14 samples in the phase-encoded dimension and 14 samples in the frequency-encoded dimension as well as square patterns spaced 2, 4 and 6 samples apart.

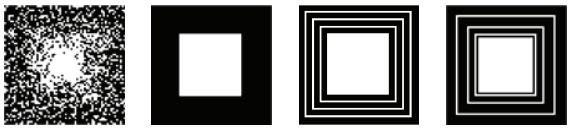

Fig. 4. A comparative example of the best sampling geometries for a minimum K-sample reduction of 60% or more. (a) PDF geometry class and provides a 60% reduction of K-space data, with a PSNR of 41.39 dB. Image (b) represents the CLP geometry and provides a 73% reduction of K-space samples, with a PSNR of 38.91 dB. Image (c) represents the SHP geometry class and provides a 59% reduction of K-space data, with a PSNR of 40.81 dB. Image (d) represents the DY geometry class and provides a 67% reduction of K-space data, with a PSNR of 38.8 dB.

TABLE I
BEST PSNR IN RANGE OF K-SPACE REDUCTION

Geometry Description	K-Space Sample Reduction	PSNR
CLP spanning ¼ of K-space in each dimension	> 90 %	32.17 dB
CLP spanning 1/3 of K-space in each dimension	80-90%	36.70 dB
SHP with CLP spanning 1/2 of K-space in each dimension and structures spaced by 12 samples	70-80%	38.92 dB
PDF with 60% reduction of K-space samples.	60-70%	41.32dB

For different percentages of K-space sample reduction, we provide a summary in Table I. From Table I, we can see how different types of geometries dominated over different data reduction rates.

C. Segmentation of Neural Activity

Using the optimal TV reconstruction coefficients, all geometries were applied to two separate fMRI data sets.

An example of a brain activity map is given in Figure 5. Segmented brain activity images were generated for each of the sampling geometries. The average error between the original segmented difference image and the reconstructed segmented difference image for each class of geometry are shown in Table II.

The most consistent reconstructions are obtained using geometries that have large low frequency regions. CLP geometries that covered less than 1/6 of the phase and frequency encoded dimensions were much less effective.

When considering all of these experiments, the geometry that provided a reconstruction PSNR greater than 30dB with a 93% reduction of K-space samples emphasize that data reduction may be the most telling of this study. This was achieved by CLP geometry with a low frequency sampling support of 25% in both the phase and frequency encoded dimensions. It is depicted left-most image in Figure 6.

The CS techniques resulted in a segmentation error of 3.125% for the first image set and 2.03% for the second image set. The sampling geometry, and reconstructed difference images, along with the original difference images for comparison, are also shown in Figure 6. The figure reveals that there is some segmentation error when the same

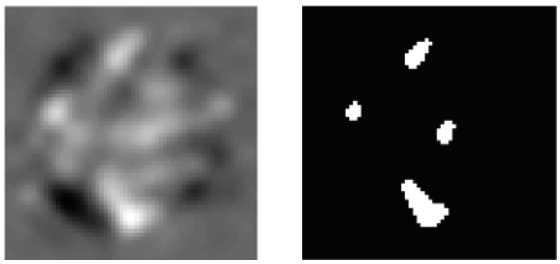

Fig. 5. An example of a brain activity map. The segmented image on the right is obtained by thresholding the image on the left using a threshold of 2 standard deviations of the image data. Binary morphology is then applied to remove any non-contiguous regions.

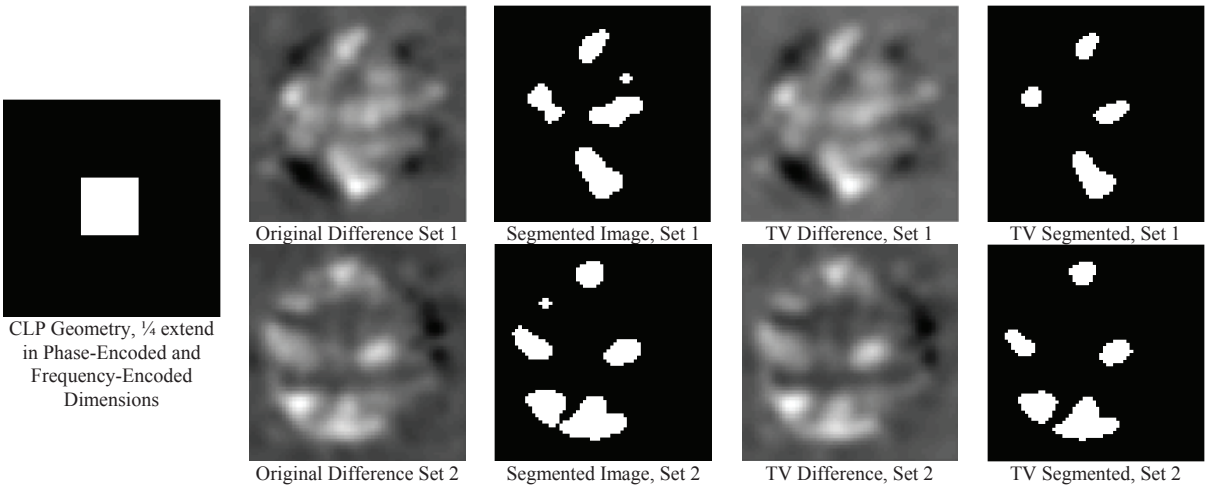

Fig. 6. The mask used in these reconstructions is from the CLP geometry class, and represents a 93% reduction in K-space data. The top row represents the first data set. The bottom row represents the second data set. The smoothed difference image and segmented image of the entire K-space data are shown first, while the TV reconstructed K-space results in the third and fourth columns. The error percentage for the first data set was 3.1%. The error percentage for the second data set was 2.32%.

threshold is set for 2-sigma of the difference image. Adjusting these threshold values can lower the segmentation error between the original difference images and the TV difference images, but only at the risk of not detecting all the pixels in which brain activity is present.

V. Conclusion

The intention of this study was to explore the feasibility of using CS reconstruction methods on low resolution fMRI data sets. Various sampling geometries were developed and explored. Adjustment of the TV coefficients resulted in boosted PSNR values, with many geometries having PSNR values over 30dB when the optimal TV coefficients were found. Difference image calculation and segmentation resulted in low (< 5%) error when segmenting the difference images of smoothed reconstructed brain slice images. Further work in this research area can seek to find better sampling geometries. Additional data sets can help determine whether or not these methods can be applied more generally.

The promising results revealed by this study have shown that CS methods may be useful in reducing the amount of data required for fMRI data collection and analysis.

TABLE II
Average Segmentation Error

Geometry Class	Avg. Number of Erroneous Pixels	Percent Error
SHP (CLP = 1/2)	88.75	2.17 %
DY	159.75	3.90%
SHP (CLP =1/4)	166.75	4.07%
SHP (CLP =1/6)	194.56	4.750%
SHP (CLP =1/8)	202.38	4.94%
SHP (CLP = 1/3)	241.44	5.89%
PDF	247.43	6.04%
SHP (CLP = 1/10)	262.94	6.42%
SHP (CLP =1/12)	286.45	6.99%
SHP (CLP =1/16)	302.38	7.38%
SHP (CLP =1/32)	463.75	11.322
CLP	742.83	18.14%

The fraction associated with each SHP geometry denotes the extend of the samples included in the DC region of the geometry in the phase-encoded and the frequency-encoded dimensions. E.g. 1/10 denotes that the CLP portion of the geometry includes 1/10 of samples along the phase-encoded dimension and 1/10 of the samples along the frequency-encoded dimension. The equally spaced square patterns create unique geometries with a constant DC support.

References

[1] M. Lustig, D.L. Donoho, J.M. Santos, and J.M. Pauly, "Compressive Sensing MRI," *IEEE Signal Processing Magazine*, 25(2), pp. 72-82, March 2008.

[2] J. Romberg, "Imaging via compressive sampling", *IEEE Signal Processing Magazine,* vol. 25, pp. 14-20, March 2008.

[3] M. Lusting, D. Donoho, and J.M. Pauly, "Sparse MRI: The application of compressed sensing for rapid MR Imaging", in *Magnetic Resonance in Medicine*, vol. 58, pp. 1182-1195, December 2007.

[4] E. Candès and M.B. Wakin, "An introduction to compressive sampling", *IEEE Signal Processing Magazine,* vol. 25, pp. 21-30, March 2008.

[5] E. Candès, J. Romberg, and T. Tao, "Robust uncertainty principles: Exact signal recovery from incomplete frequency information", *IEEE Trans. Information Theory,* vol. 52, pp. 489-509, February 2006.

[6] G.J. Marseille, R. de Beer, M. Fuderer, A.F. Mehlkopf, and D. van Ormondt, "Nonuniform phase-encoded distributions for MRI scan time reduction", *Journal of Magnetic Resonance*, vol. 111, pp. 70-75, 1996.

[7] C.M. Tsai and D. Nishimura, "Reduced aliasing artifacts using variable-density K-space sampling trajectories", in *Magnetic Resonance in Medicine,* vol. 43, pp, 452-458, 2000.

[8] A. Greiser and M. von Kienlin, "Efficient K-space sampling by density-weighted phase-encoding", in *Magnetic Resonance in Medicine,* vol. 50, pp. 1266-1275, 2003.

[9] Y. Tsaig and D.L. Donoho, "Extensions of compressed sensing," in *Signal Processing*, vol. 86, pp. 533-548, 2006.